Correction of Computed Tomography Motion Artifacts Using Pixel-Specific Back-Projection

Cameron J. Ritchie,* Carl R. Crawford, *Senior Member, IEEE*, J. David Godwin, Kevin F. King, and Yongmin Kim, *Fellow, IEEE*

Abstract—**Cardiac and respiratory motion can cause artifacts in computed tomography scans of the chest. We describe a new method for reducing these artifacts called pixel-specific back-projection (PSBP). PSBP reduces artifacts caused by in-plane motion by reconstructing each pixel in a frame of reference that moves with the in-plane motion in the volume being scanned. The motion of the frame of reference is specified by constructing maps that describe the motion of each pixel in the image at the time each projection was measured; these maps are based on measurements of the in-plane motion. PSBP has been tested in computer simulations and with volunteer data. In computer simulations, PSBP removed the structured artifacts caused by motion. In scans of two volunteers, PSBP reduced doubling and streaking in chest scans to a level that made the images clinically useful. PSBP corrections of liver scans were less satisfactory because the motion of the liver is predominantly superior–inferior (S–I). PSBP uses a unique set of motion parameters to describe the motion at each point in the chest as opposed to requiring that the motion be described by a single set of parameters. Therefore, PSBP may be more useful in correcting clinical scans than are other correction techniques previously described.**

I. Introduction

CARDIAC and respiratory motion causes artifacts in computed tomography (CT) scans of the chest [1], [2]. These artifacts are clinically significant because they may obscure pathology [3] or mimic disease [4]. These artifacts can be reduced or eliminated using fast scanning [5], gating [6], *underscan* [7], *overscan* [8], *halfscan* [9], or corrective reconstruction [10]. Although each technique has merit [11], we will consider only corrective reconstruction in this paper.

Motion artifacts in chest scans in magnetic resonance imaging (MRI) have been reduced by first describing motion with a parametric model and then modifying the reconstruction algorithm to correct for the modeled motion [12]–[15]. Crawford *et al.* [10] adapted this idea to CT reconstruction by deriving a filtered back-projection algorithm that corrected for motion in the chest that fit a time-varying expansion model (we denote this algorithm CTX). Using CTX, the effects of motion could be completely removed when the object function's motion fit the assumed model. The key to CTX correction was that the back-projection was performed in a frame of reference that moved according to the motion model. However, CTX's usefulness was limited by the fact that motion in the chest did not correspond to a time-varying magnification.

A more physiologically correct model for respiratory motion is one in which points in the posterior portion of the chest remain essentially stationary while those above the midline expand approximately radially [16]. Cardiac motion causes points in the left chest to move radially from the mediastinum. Additionally, there is motion in the superior–inferior (S–I) direction caused by diaphragmatic breathing and heartbeat. This S–I motion is difficult to measure, and thus it is difficult to correct. Therefore, all of the correction algorithms described here are applicable only superior to the heart midline where the S–I motion caused by diaphragmatic and left-ventricular motion is minimal.

Maeda *et al.* [17] demonstrated that in MRI, the point-spread function is space-invariant in the absence of off-resonant spins. A consequence of this result (for blur caused by off-resonance with non-Cartesian k-space trajectories) is that for an on-resonance receiver, the image point is not corrupted by artifacts from neighboring points that are at different local frequencies. Noll *et al.* [18] used this result to develop a localized correction method for removing blurring in MRI images caused by off-resonance. Noll *et al.* used an autofocus technique to estimate unique correction parameters for each point in the image. They demonstrated that correction of points using locally estimated parameters did not create artifacts in adjacent regions that would recontaminate the target region. Ehman *et al.* [13] also used the results of Maeda *et al.* to develop a motion artifact correction method for MRI in which the correction was performed on a localized basis. However, their method relied on a time-varying magnification model of motion in the chest to estimate the motion of each point.

CTX's usefulness was limited by the fact that the time-varying magnification model was not valid for motion in the chest. For the type of motion that does occur in the chest, an exact filtered back-projection algorithm could not be derived. Noll *et al.* found that some types of artifact correction benefited from estimating correction parameters for small regions and

Manuscript received March 27, 1995; revised February 1, 1996. The Associate Editor responsible for coordinating the review of this paper and recommending its publication was M. Vannier. *Asterisk indicates corresponding author.*

*C. J. Ritchie was with the University of Washington, Department of Bioengineering, Seattle, WA 98195 USA. He is now with Imatron, Inc., 389 Oyster Point Blvd., South San Francisco, CA 94080 USA (e-mail: cameron_ritchie@imatron.com).

C. R. Crawford is with the University of Washington, Department of Radiology, Seattle, WA 98195 USA. He is also with G. E. Medical Systems, Milwaukee, WI 53201 USA and the University of Washington, Department of Electrical Engineering, Seattle, WA 98195 USA.

J. D. Godwin is with the University of Washington, Department of Radiology, Seattle, WA 98195 USA.

K. F. King is with G. E. Medical Systems, Milwaukee, WI 53201 USA.

Y. Kim is with the University of Washington, Department of Electrical Engineering, Seattle, WA 98195 USA.

Publisher Item Identifier S 0278-0062(96)04239-5.

then applying the correction locally. We have extrapolated this local correction idea from MRI to CT and developed a motion artifact correction algorithm in which the CTX time-varying model is applied on a local basis, and in which unique CTX model parameters are estimated for each point. We denote this algorithm pixel-specific back-projection (PSBP). To make PSBP useful, a method for estimating the local CTX model parameters was required. Therefore, we have also developed a method for estimating the in-plane motion of every pixel in the image at the time each projection is measured.

The PSBP algorithm is heuristic in that we have not proven mathematically that the correction of one point is not corrupted by artifacts from neighboring points. Therefore, we make the assumption in PSBP that local correction is valid. Through experimentation, we have confirmed that this assumption appears to be true. PSBP was tested in computer simulations and on volunteer data. For the computer simulations, PSBP reconstructions of projections taken from a moving test object eliminated all motion artifacts. For the volunteer data, PSBP reconstructions of chest scans taken from spontaneously breathing volunteers reduced doubling of vessels and blurring.

This paper is organized as follows. In Section II, we give a brief description of the CTX algorithm. In Section III, we describe PSBP. In Section IV, we describe our method for extracting the in-plane motion. In Sections V and VI, we show the results of applying PSBP to computer-simulated and volunteer projection data, respectively.

II. Description of CTX

The CTX algorithm reduces motion artifacts by performing the back-projection in a frame of reference that moves with the object. The motion during scanning is modeled as a shift and as a magnification about some origin point (x_0, y_0). CTX uses projection data during back-projection that corresponds to the location at which each point resided at the time each projection was measured.

In CTX, let $f(x,y)$ be the cross section that is to be reconstructed. A magnified and shifted version of $f(x,y)$, $f'(x,y)$ is given by

$$f'(x,y) = f(\alpha_x + \beta_x x, \alpha_y + \beta_y y) \tag{1}$$

where α_x and α_y are shift factors, and β_x and β_y are magnification factors. Both the α's and the β's are assumed to be functions of projection angle θ, which is in turn a function of time. The direction of the z axis is assumed to be the superior-inferior direction, and the z axis is perpendicular to the xy-image plane.

A parallel projection $P'(\theta,t)$ of $f'(x,y)$ is given by the radon transform

$$P'(\theta,t) = \int_{-\infty}^{\infty}\int_{-\infty}^{\infty} f'(x,y)\delta(t - x\cos\theta - y\sin\theta)dxdy \tag{2}$$

where $\delta(t)$ is a Dirac-delta distribution, and t is the detector position within the projection. Substituting (1) in (2) and computing the Fourier transform (FT) of $P'(\theta,t)$ yields

$$S'(\theta,\omega) = \int_{-\infty}^{\infty}\int_{-\infty}^{\infty} f(\alpha_x + \beta_x x, \alpha_y + \beta_y y) \times e^{-j2\pi\omega(x\cos\theta + y\sin\theta)}dxdy \tag{3}$$

where $S'(\theta,\omega)$ is the projection's FT. The change of variables

$$x' = \alpha_x + \beta_x x \tag{4}$$

$$y' = \alpha_y + \beta_y y \tag{5}$$

can now be made in (3) which yields

$$S'(\theta,\omega) = \int_{-\infty}^{\infty}\int_{-\infty}^{\infty} \frac{f(x',y')}{\beta_x\beta_y} e^{-j2\pi\omega\left[\frac{x'}{\beta_x}\cos\theta + \frac{y'}{\beta_y}\sin\theta\right]} \times e^{j2\pi\omega\left[\frac{\alpha_x}{\beta_x}\cos\theta + \frac{\alpha_y}{\beta_y}\sin\theta\right]}dx'dy'. \tag{6}$$

By noting that the first two terms of (6) describe the two-dimensional (2-D) FT of the function $f(x',y')$, (6) can be rewritten

$$S'(\theta,\omega) = \frac{e^{j2\pi\omega\left[\frac{\alpha_x}{\beta_x}\cos\theta + \frac{\alpha_y}{\beta_y}\sin\theta\right]}}{\beta_x\beta_y} \times F\left(\frac{\omega\cos\theta}{\beta_x}, \frac{\omega\sin\theta}{\beta_y}\right) \tag{7}$$

where $F(u,v)$ is the 2-D FT. Equation (7) shows that the one-dimensional (1-D) FT of the projection $P'(\theta,t)$ is equal to a spoke of the 2-D FT of the magnified-and-shifted object function $f(x',y')$ at angle θ', where θ' is given by

$$\theta' = \tan^{-1}\left[\frac{\beta_x}{\beta_y}\tan\theta\right]. \tag{8}$$

The expression for the inverse FT of the function $F(u,v)$ is given by

$$f(x,y) = \int_{-\infty}^{\infty}\int_{-\infty}^{\infty} F(u,v)e^{j2\pi(ux+vy)}dudv. \tag{9}$$

Consider the following change of variables

$$u = \frac{\omega}{\beta_x}\cos\theta \tag{10}$$

$$v = \frac{\omega}{\beta_y}\sin\theta. \tag{11}$$

The Jacobian $J(u,v;\omega,\theta)$ for this change of variables reduces to

$$J(x,y;\omega,\theta) = \frac{|\omega|g(\theta)}{\beta_x\beta_y} \tag{12}$$

where $|\omega|$ is the filter function, and $g(\theta)$ is given by

$$g(\theta) = \left|1 + \frac{\sin 2\theta}{2}\left(\frac{\beta_{x\theta}}{\beta_x} - \frac{\beta_{y\theta}}{\beta_y}\right)\right| \tag{13}$$

and where $\beta_{x\theta}$ and $\beta_{y\theta}$ are the partial derivatives of β_x and β_y with respect to θ.

Substituting (10) through (13) into (9) yields

$$f(x,y) = \int_0^{\pi}\int_{-\infty}^{\infty} F\left(\frac{\omega\cos\theta}{\beta_x}, \frac{\omega\sin\theta}{\beta_y}\right) \times \frac{|\omega|g(\theta)}{\beta_x\beta_y} e^{j2\pi\omega\left[\frac{x}{\beta_x}\cos\theta + \frac{y}{\beta_y}\sin\theta\right]}d\omega d\theta \tag{14}$$

where the limits of integration have been changed because θ is periodic with a period of π. Now, a reconstruction formula for a magnified and shifted object can be obtained by substituting (7) into (14), which, after simplification yields

$$f(x,y) = \int_0^{\pi} q_\theta\left(\left[\frac{x-\alpha_x}{\beta_x}\right]\cos\theta + \left[\frac{y-\alpha_y}{\beta_y}\right]\sin\theta\right)d\theta \tag{15}$$

where $q_\theta(t)$ is the filtered projection of $f(x',y')$, which is defined as

$$q_\theta(t) = \int_{-\infty}^{\infty} S'(\theta,\omega)|\omega|g(\theta)e^{j2\pi\omega t}d\omega. \tag{16}$$

The reconstruction formula in (15) shows that $f(x,y)$ can be completely recovered from projections acquired from $f'(x,y)$. Equations (1)–(16) describe the CTX algorithm for parallel projections. The fan-beam derivation is similar to the parallel derivation except that one must make the approximation that if the fan-beam data was rebinned into parallel projections, the magnification and shift factors would be independent of detector position. As shown in [10], this assumption is reliable if the motion is slowly varying.

III. Description of PSBP

Although the CTX algorithm is mathematically correct, it is based on a model that does not describe motion in the chest. Furthermore, an exact back-projection algorithm could not be derived that accounted for this motion. Therefore, we made the assumption that the CTX model was valid only in a small region around each pixel, and that the α and β parameters of the CTX model for each of these regions need not be identical. We then developed an algorithm in which each pixel was reconstructed in a frame of reference local to that pixel. To develop such an algorithm, we made the assumption that local correction was valid in CT reconstruction.

To perform local correction, the motion in a body is first described by a temporally and spatially varying function (called a warping function). These warping functions are, in general, a function of space and projection angle

$$\begin{aligned} x' &= G(x,y,\theta) \\ y' &= H(x,y,\theta) \end{aligned} \tag{17}$$

where (x',y') are the warped Cartesian coordinates, (x,y) are the nonwarped coordinates, θ is the projection angle, and G and H are the warping functions.

To apply the correction method of CTX on a local basis, the general warping functions in (17) need to be approximated for each pixel to match the magnification and shift model of (1). To make this approximation, the α and β values need to be extracted from the generic functions G and H. To perform this extraction, first consider the 1-D case of two points being magnified and shifted in the x direction. The first point, x_1, would move to a new location, $x_1{}'$, as given by

$$x_1' = \alpha_x + \beta_x x_1 \tag{18}$$

while the point x_2 would move to location x_2' as given by

$$x_2' = \alpha_x + \beta_x x_2 \tag{19}$$

where the α's and β's are the same in both equations. Combining (18) and (19) and solving for β_x yields

$$\beta_x = \frac{x_1' - x_2'}{x_1 - x_2}. \tag{20}$$

Substituting (20) back into (18) yields an expression for α_x

$$\alpha_x = \frac{x_1 x_2' - x_2 x_1'}{x_1 - x_2}. \tag{21}$$

In the general case, $x_1{}' = f(x_1)$ and $x_2{}' = f(x_2)$, where f is an arbitrary function. Making this change in (20) and (21), and then allowing the distance between x_1 and x_2 to go to zero reveals that α_x and β_x become functions of derivatives of f. If the 1-D function f is now replaced with G (and H) from (17), the full derivatives become partial derivatives, and

$$\begin{aligned} \beta_x &= \frac{\partial G}{\partial x} \\ \beta_y &= \frac{\partial H}{\partial y} \end{aligned} \tag{22}$$

and

$$\begin{aligned} \alpha_x &= G - \frac{\partial G}{\partial x} \\ \alpha_y &= H - \frac{\partial H}{\partial y} \end{aligned} \tag{23}$$

where α_y and β_y have been added because their derivation is identical.

If our assumptions on the validity of local correction hold, then the pixel (x,y) can now be reconstructed as shown in (15) where the α and β values are defined as in (22) and (23). However, using (22) and (23) in (15) only approximates G and H. Therefore, (15) should be rewritten using the exact inverses of the warping functions

$$\begin{aligned} f(x,y) = \int_{-\infty}^{\infty} q_\theta([G^{-1}(x,y,\theta)]\cos\theta \\ + [H^{-1}(x,y,\theta)]\sin\theta)d\theta \end{aligned} \tag{24}$$

where the functions $q_\theta(t)$ and $g(\theta)$ are defined as in (16) and (13).

Equations (24), (16), and (13) describe how an image of the object function $f(x,y)$ can be reconstructed from projections of the warped object function $f(x',y')$ if the assumption of local correction is valid. As was the case with the CTX discussion, (17)–(24) describe PSBP for parallel-beam projections. The fan-beam derivation is similar to the parallel derivation except that one must make the approximation that if the fan-beam data were rebinned into parallel projections, the magnification and shift factors would be independent of detector position.

IV. Motion Tracking

Because PSBP corrects for motion on a pixel-by-pixel basis, the in-plane motion of every pixel must be known before PSBP

can be used to reduce motion artifacts in CT scans. Therefore, we developed a two-part tracking method that could generate a detailed description of the motion in the chest. In part one, we measure the position and displacement during scanning of identifiable points in the chest such as ribs and blood vessels. These points are denoted *node points*. We used two different methods for selecting and measuring node points depending on the type of motion artifact present in the image. In part two, we constructed motion maps that estimated the position of every point in the chest at the time that every projection was measured by spatially and temporally interpolating between the node points.

A. Node Points

We developed two methods for measuring the in-plane motion of node points that occurred during scanning. For scans in which the artifacts manifested mainly as blurring and streaking, a full revolution of data were reconstructed into overlapping halfscans, and the positions of moving structures were recorded in each halfscan. This method is denoted the *halfscan* method. For scans in which the motion caused streaking artifacts in halfscans that interfered with node point measurement, use of the halfscan method was precluded, and instead the in-plane motion of node-points was estimated by first reconstructing the projections with a conventional back-projection algorithm and then determining the distance between duplicated structures on the image. This method is denoted the *doubled-structure method.*

For the halfscan method, we reconstructed multiple halfscans from a single revolution of projection data by incrementing the starting angle of each halfscan. Typically, two or three degrees separated the halfscan starting angles. Therefore, because projection angle is proportional to time, the location of structures in each halfscan represented the average position of the structure over the time taken to acquire the projections from which the halfscan was reconstructed. Therefore, we arbitrarily specified that the position of each structure in each halfscan corresponded to the location of the structure at the time that the center projection of the halfscan was acquired. Because positions were temporally located at the time of the midpoint of the halfscan, no position data existed for times before the midpoint of the first halfscan or after the midpoint of the last halfscan. To estimate the positions of node points for these times, linear extrapolation was used.

In each halfscan, the positions of structures such as the ribs, the sternum, the vertebrae, the pulmonary vessels, the heart wall, and the chest wall were recorded by analyzing the image with image processing software (Image 1.47, National Institutes of Health). For structures that appeared as points such as vessels imaged in cross section or a recognizable point on the chest wall, the (x, y) coordinates of the structure were recorded by placing a cursor over the structure. For structures that were larger than points (such as a rib), the image was first thresholded so that the structure of interest was above the threshold, and then the image processing software's region growing function was used to segment the structure. After segmentation, the software computed the (x, y) coordinates of the structure's center-of-mass. The (x, y) coordinates of the center-of-mass were used to define the structure's position.

For the doubled-structure method, we selected doubled structures such as vessels, the heart wall, or the sternum as node points and estimated the node's displacements by measuring the distance between the two appearances of the same structure. The first appearance was taken as the average position of the node during the first half of the scan, and the second appearance as the average position during the second half of the scan. Positions at times between these two endpoints were estimated by linearly interpolating between the values. An inherent difficulty with this approach is that it will tend to overestimate the velocity of motion during the course of scanning. For this reason, we only used the doubled-structure method when artifacts were so severe that use of the halfscan method was precluded.

For each volunteer image presented in this paper, approximately 15 points were identified as node points. We attempted to choose points so that node points were spread uniformly over the image. However, we were forced to use points that we were able to follow over the course of the halfscans, or that demonstrated doubling. Therefore, we were not always free to select points uniformly over the image.

B. Motion Maps

After node points had been measured using either the halfscan or the doubled-structure methods, we computed the displacement of the point at the time of each projection. The x and y displacement of each node point was determined by subtracting the present position of the node from its position at the time that the first projection was acquired. This first projection is denoted a reference projection. Two grids, equal in size to the image grid, were then created, and the x or y displacement of each node point was placed on the grid at the (x, y) reference location of the node point. These grids are called x- and y-motion maps (denoted M_x and M_y).

To estimate the displacements of all the points in the motion maps that were not node points, we performed a three-point interpolation. For each point (x, y) that was not a node point, the three node points nearest to (x, y) that formed a triangle that enclosed (x, y) were selected. This selection was performed by first finding the three node points nearest to the point (x, y) and then determining if these three node points formed a triangle that enclosed (x, y). If the three nearest node points did not form a suitable triangle, we then replaced each node point in the original triad with the fourth nearest node point, and repeated the triangle calculations. This procedure was repeated until a suitable triangle was formed. The interpolation was then performed by fitting a plane through the three selected node points and evaluating the equation of the plane at (x, y).

To ensure that all (x, y) were surrounded by at least three node points, we added node points at the edges of the motion maps prior to beginning the three-point interpolation process. These added node points were called synthetic node points to distinguish them from actual node points that were obtained by measuring the displacements of structures in halfscans. Five

synthetic node points were added along each edge of each map, and the displacement of these points was set equal to 75% of the displacement of the nearest actual node point. The 75% value was arrived at empirically by noting that this value eliminated doubling artifacts of the anterior surface of the chest wall. This 75% value is specific to a field-of-view (FOV) larger than 40 cm; for smaller FOV's, a different value would have to be empirically determined.

We found empirically that removing the discontinuities that arose along the borders of planes improved the motion artifact correction. Therefore, the maps were convolved with a 9×9 averaging kernel [kernel computed the simple average of the pixel values in the 9×9 region around (x, y)]. The size of the kernel was determined empirically by visually comparing images reconstructed with kernels of different sizes.

Motion maps were created at every time for which node point data existed. Temporally, this set of motion maps defined the displacement of every pixel at the time that the middle projection of each halfscan was acquired. However, the displacements of every pixel at the time that every projection was measured was required. Therefore, to form a motion map for each projection angle θ for which a motion map did not already exist, we linearly interpolated between the nearest existing motion maps.

The set of motion-map functions M_x and M_y describe the motion of every point in image space at the time that every projection was acquired. To obtain the warped coordinates of any point in the image plane, the displacement in the motion map is added to the position of the point the time at which the reference projection was acquired

$$\begin{aligned} x' &= x_0 + M_x(x, y, \theta) \\ y' &= y_0 + M_y(x, y, \theta) \end{aligned} \tag{25}$$

where (x', y') is the warped position of any point, and (x_0, y_0) is the position of the point at the reference time. Equation (25) is the discrete representation of G and H as described in (17), and can thus be used with PSBP.

V. Computer Simulations

We performed computer simulations to test both PSBP and our motion tracking algorithm. To test PSBP, we reconstructed projections of a warped object using PSBP and the exact inverses of the warping functions. To test motion tracking, we created projections of an object undergoing motion, tracked the motion, and then reconstructed images using PSBP and the tracking data.

A. PSBP

We first developed specific examples of the warping functions G and H. These functions described a radial magnification of all points in the object around an origin point located at the posterior edge of the object. This warping function was chosen because it approximated respiratory motion [16]. We then made computer-simulated scans of a test object while it was warped according to these functions and reconstructed the images with a conventional algorithm and with PSBP.

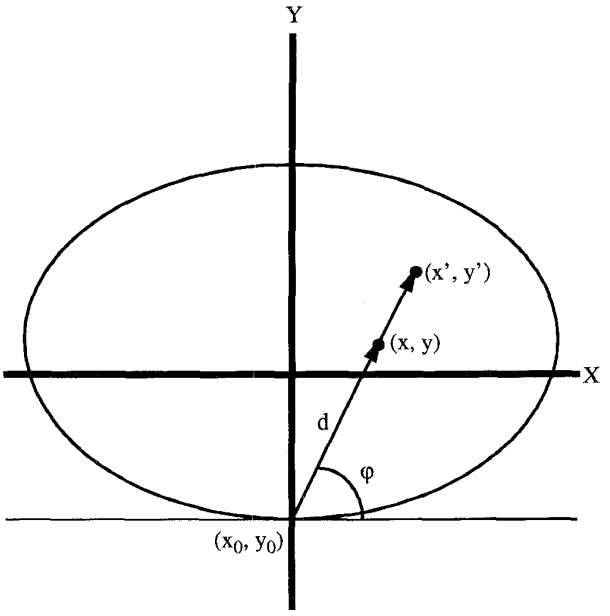

Fig. 1. Diagram of the radial warping motion model used in computer simulations.

The warping functions consisted of an angularly, spatially and temporally varying magnification about the point (x_0, y_0) on the posterior edge of the test object

$$G(x, y, \theta) = x' = d\left[\frac{m_\theta \cos\varphi}{m_\theta - (m_\theta - 1)\sin\varphi}\right] \tag{26}$$

and

$$H(x, y, \theta) = y' = d\left[\frac{m_\theta \sin\varphi}{m_\theta - (m_\theta - 1)\sin\varphi}\right] \tag{27}$$

where the terms in square brackets are magnification functions, d is the distance between the origin and the point being warped, φ is the polar angle between the ray going through (x, y) and (x_0, y_0), and m_θ is designated the magnification function

$$m_\theta = \frac{\text{FOV}}{\text{FOV} - \frac{\theta}{\pi} r}. \tag{28}$$

In (28), θ is the projection angle, FOV is the size of the field-of-view, and r is the maximum motion of the most anterior point on the test object. As shown in Fig. 1, the warp described in (26) and (27) specifies that the new position of (x, y), (x', y'), is computed by moving the point along the ray connecting (x, y) and (x_0, y_0) an amount that is proportional to the distance between (x_0, y_0) and (x, y).

To compute the Jacobian function for (26) and (27), (22) was used, yielding

$$\beta_x = \frac{m_\theta}{M}\left[1 - \frac{(m_\theta - 1)\cos^2\theta \sin\varphi}{M}\right] \tag{29}$$

and

$$\beta_y = \frac{m_\theta}{M}\left[1 - \frac{(m_\theta - 1)(y - y_0)\cos^2\theta}{m_\theta d}\right] \tag{30}$$

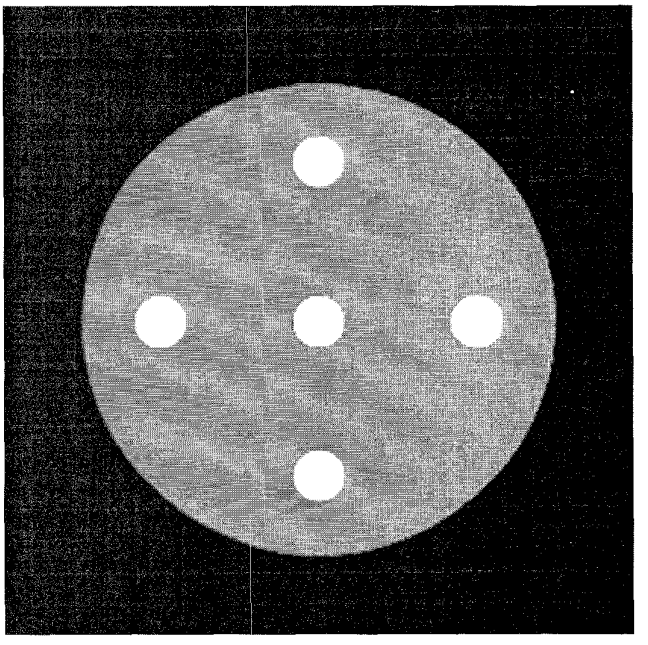

Fig. 2. Object used in computer simulations to verify theory behind PSBP.

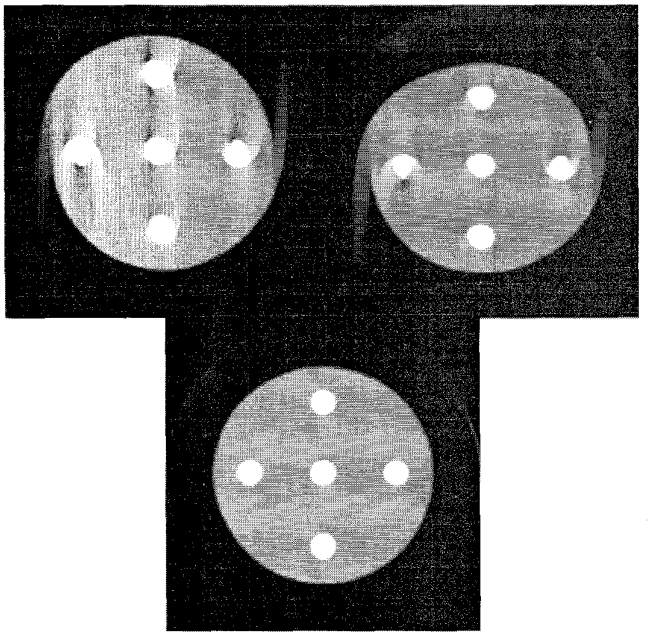

Fig. 3. Computer simulations for radial warping function during acquisition. Data for correction comes from *a priori* knowledge of the motion: (a) top left—conventional reconstruction, (b) top right—CTX reconstruction, (c) bottom—PSBP reconstruction. For all images: window = 1000 HU; level = 0 HU.

where M is given by

$$M = m_\theta - \frac{(m_\theta - 1)(y - y_0)}{d}. \tag{31}$$

The derivatives with respect to θ of these β values were complicated, and therefore remaining calculations for the $g(\theta)$ term in (13) were done using the computer program Mathematica (Wolfram Research Inc., Champaign IL).

To test PSBP using the warping functions in (26) and (27), an image of a test object was first generated with no warping. This image, shown in Fig. 2, was denoted the static image. Parallel reprojections of the static image were then obtained while the pixels were moved according to (26) and (27). Reprojection was used because the positions of individual pixels could be specified in the reprojector. The warping motion was defined so that a point on the y axis 10 mm below the top edge of the FOV was warped to the edge of the FOV at the time of the final projection. This value was chosen to simulate the chest wall motion of a quietly breathing subject. The projections were filtered and backprojected with and without underscan using a conventional back-projection algorithm, CTX, and PSBP.

Simulation images consisted of a 256^2 matrix, reconstructed from 256 parallel projections spanning 360°, and 351 samples per projection. The FOV was 10 cm. The simulated scanner had a 630-mm source-to-center distance, a 1100-mm source-to-detector distance, a point source, and point detectors. The first projection was taken with the source at the top of the reconstruction circle, and parallel projections were acquired in a counter-clockwise direction. The choice of simulation parameters was made as a compromise between clinical reality and computation time. The pixel size in these simulations was equal to that in a real scan of a thorax (40-cm FOV, 512^2 matrix); however, computation time was reduced by choosing a small matrix and a small number of samples per projection.

As shown in Fig. 3(a), images reconstructed with a conventional algorithm showed severe motion artifacts around the high-density points, black voids adjacent to each high-density circle, and vertical streaking. When CTX back-projection was used, the object boundary was partially restored to its original circular shape and some black voids were eliminated, but new voids were introduced around the left and right high-density points as shown in Fig. 3(b). When PSBP was used, the dark void artifacts and the streaking around the vertical high-density points were completely removed as shown in Fig. 3(c); however, some light vertical streaking was introduced.

We then repeated the reconstructions of the projections from the object moving according to (26) and (27) using underscan. When the standard algorithm with underscan was used, streaking and black voids were reduced as shown in Fig. 4(a), but doubling of the object boundary and distortion of the high-density ellipses were still apparent. When CTX with underscan was used, streaking artifacts were reduced as compared to Fig. 3(b), but the image was still distorted as shown in Fig. 4(b). When PSBP with underscan was used, voids and distortions were completely removed as shown in Fig. 4(c), as was the vertical streaking apparent in Fig. 3(c).

B. Motion Tracking

To determine if the our motion-tracking method accurately measured the displacements that occurred during scanning, motion tracking was applied to computer-simulated projec-

TABLE I
DIFFERENCE BETWEEN TRACKED AND MEASURED MOTIONS

Ellipse Number	X			Y		
	Peak-to-Peak Motion (mm)	Actual - Measured		Peak-to-Peak Motion (mm)	Actual - Measured	
		Mean (mm)	Std. Dev. (mm)		Mean (mm)	Std. Dev. (mm)
1	0.134	0.223	0.468	6.299	1.286	0.693
2	0.078	0.075	0.791	8.387	0.692	1.005
3	0.000	-0.054	1.383	8.944	-0.374	1.179
4	-0.078	0.097	0.898	8.387	-1.449	0.951
5	-0.134	-0.341	0.404	6.299	-1.753	0.755

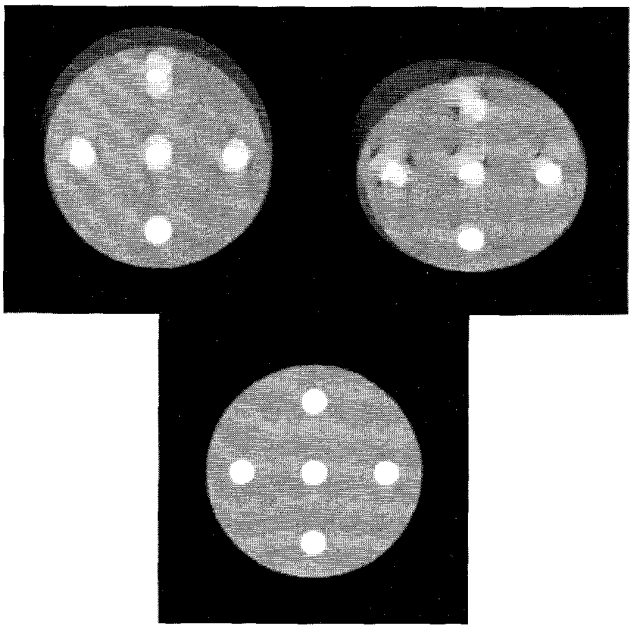

Fig. 4. Computer simulations for radial warping function during acquisition. Data for correction comes from *a priori* knowledge of the motion: (a) Top left—conventional reconstruction with underscan, (b) top right—CTX reconstruction with underscan, and (c) bottom—PSBP reconstruction with underscan. For all images: window = 1000 HU; level = 0 HU.

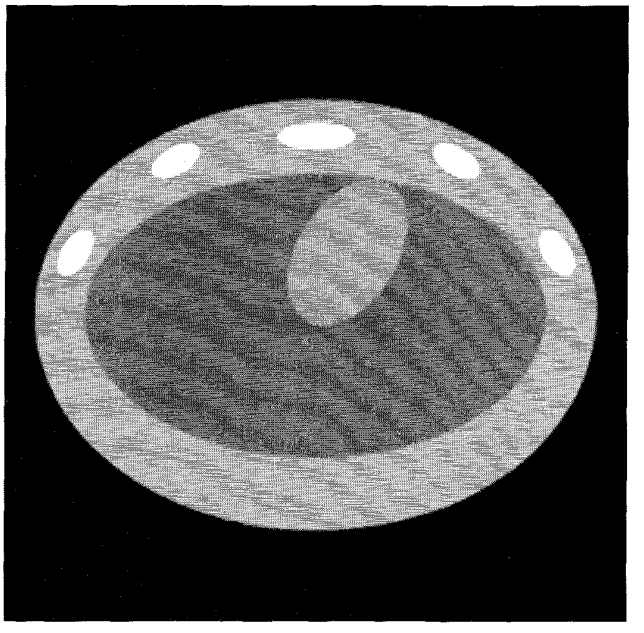

Fig. 5. Object used in computer simulations to verify PSBP combined with motion tracking.

tions. The performance of the motion-tracking algorithm was evaluated directly by comparing actual motion to motion measured with tracking, and indirectly by comparing reconstructions made with PSBP and the tracking data. We used the halfscan method to identify and measure node points.

Computer-simulated scans of a moving test object were performed. The test object is shown in Fig. 5. Points in the test object were warped about a point on the posterior edge of the large ellipse according to (26) and (27). A maximum motion of 10 mm was specified. One revolution (2π) of equal-space fan-beam projection data were generated from the moving test object. Simulation parameters were 256 projections per revolution, 351 samples per projection, 100-mm radius FOV, and a 256^2 reconstruction grid. The fan angle for this geometry was 10°, and thus each halfscan required 200° of projection data. The dimension of time was added to the computer simulations by adjusting the motion parameters so that the amount of motion that would occur in a 1- or 2-s scan of a normally breathing volunteer was approximated [16]. Time was added to these simulations so that we could assess the effect of larger amounts of motion (in the longer scans) on the quality of the motion tracking. From the projection data, halfscans were reconstructed every 5°. The displacements of five node points corresponding to the high-density ellipses in the test object were tracked, and motion maps were formed.

For the simulated 1-s scans, the motion-tracking algorithm was evaluated directly by comparing actual motions to measured motions for the five node points. Referring to Fig. 5, the node points were first numbered from left to right. The difference between the actual and measured positions of each node point in both the x and y directions was computed as a function of projection angle. The mean and standard deviations of these differences, along with the actual maximum motion of each node point is given in Table I.

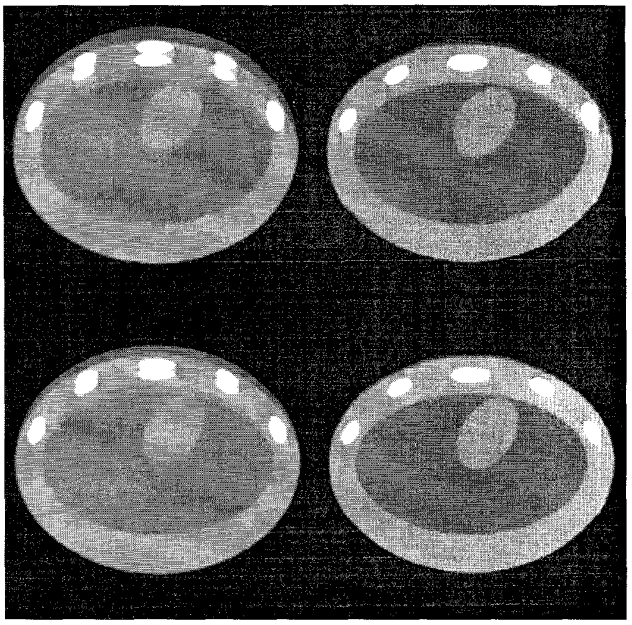

Fig. 6. Computer simulations for radial warping function during acquisition. Data for correction comes from motion tracking: (a) top left—2-s scan, conventional reconstruction, (b) top right—2-s scan, PSBP reconstruction, (c) bottom left—1-s scan, conventional reconstruction, and (d) bottom right—1-s scan, PSBP reconstruction. For all images: window = 1000 HU; level = 0 HU.

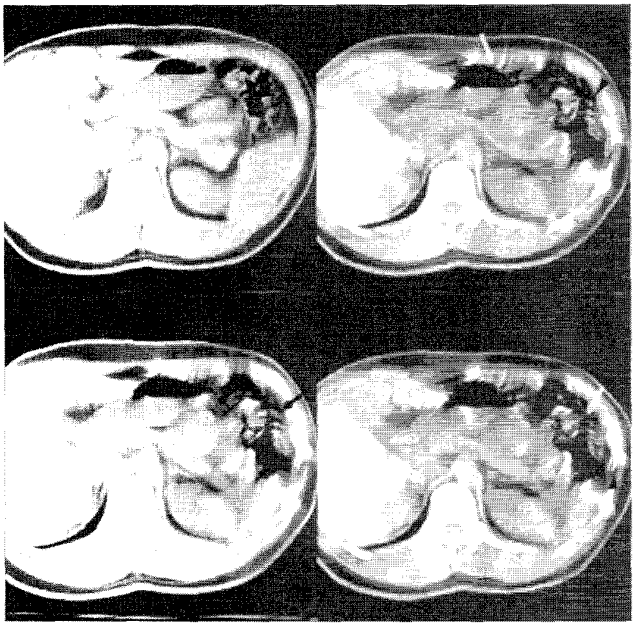

Fig. 7. Scans through the liver from volunteer 1: (a) top left—Scan during breath hold, (b) top right—scan during exhalation showing streaking and doubling, (c) bottom left—scan in (b) reconstructed with CTX, and (c) bottom right—scan in (b) reconstructed with PSBP. For all images: window = 200 HU; level = −200 HU.

For both the simulated 1-s and the simulated 2-s scans, the motion-tracking algorithm was evaluated indirectly by comparing reconstructions of the projections of the moving object using a standard algorithm to reconstructions using PSBP and the motion-tracking information. Underscan was not used. Using PSBP and the tracking data removed streaking artifacts and restored the test object boundary, as shown in Fig. 6. As expected, corrections of 1-s scans contained fewer streaking artifacts than corrections of 2-s scans because less motion occurred in the shorter scans.

VI. Volunteer Scanning

PSBP and the motion tracking algorithm were tested on scans of two volunteers. For the first volunteer, scans were obtained through the liver just below the diaphragm and through the base of the lung. At each level, the volunteer was first scanned while holding his breath, and then he was scanned again while he exhaled a deep breath. Scan time was 4.0 s. For the second volunteer, scans were obtained through the base of the lung only. The volunteer was scanned while breathing spontaneously, and no breath-holding image was obtained, although images obtained at end-expiration contained few motion artifacts. The image to be corrected was obtained during exhalation. Scan time was 1.0 s. The three levels from the volunteers were first reconstructed with a conventional algorithm. The images were then reconstructed with CTX and PSBP. Underscan was not used for the PSBP reconstructions.

In the first volunteer (Figs. 7 and 8), full-range respiratory motion occurred during scanning which caused streaking artifacts around node points such as the ribs as shown in Fig. 7. Therefore, the doubled-structure node point method was used for motion tracking. In the second volunteer, quiet breathing occurred during scanning, and thus streaking was not problematic as shown in Fig. 9. Therefore, the halfscan node point method was used for motion tracking; halfscans with start-angles every 5° were reconstructed.

For the scan through the liver, the scan during breath-holding showed the abdominal wall as a single structure, and intestinal gas appears as black patches as shown in Fig. 7(a). The scan during exhalation reconstructed with a conventional algorithm showed streaking from the fluid-air interface (arrows), and the black patches corresponding to gas bubbles in the colon are severely distorted (arrowheads) as shown in Fig. 7(b). The scan during exhalation reconstructed with CTX showed streaking; however, the streaking and distortions around the gas bubbles are slightly less severe (arrows) as shown in Fig. 7(c). In addition, doubling beneath the anterior surface of the abdominal wall is reduced. The scan during exhalation reconstructed with PSBP showed the same streaking as in the CTX image; however, the distortions around the gas bubbles are slightly less severe (arrows), and the rib to the right of the air bubbles is now visible (arrowhead) as shown in Fig. 7(d).

For the scans through the lung from the first volunteer, the scan during breath-holding showed the chest wall and the pulmonary vessels as well-defined structures as can be seen in Fig. 8(a). The scan during exhalation reconstructed with a conventional algorithm showed dark patches in the lower right lung, and severe doubling of the chest wall and

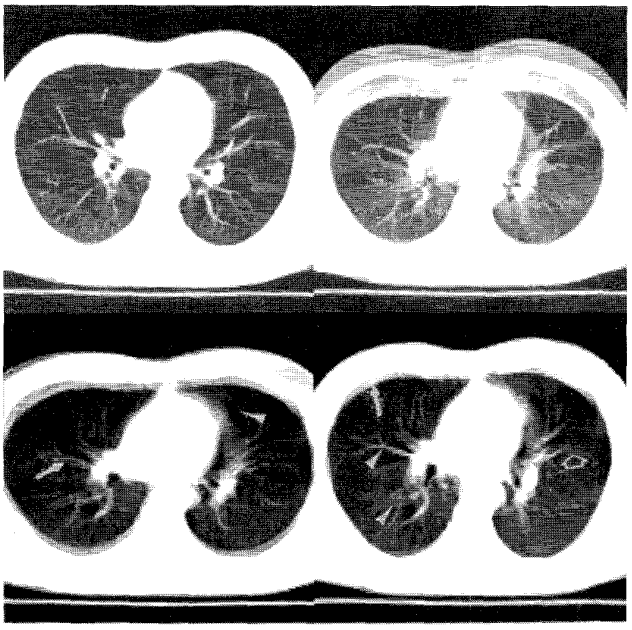

Fig. 8. Scans through the chest from volunteer 1: (a) top left—Scan during breath hold, (b) top right—scan during exhalation. (c) bottom left—scan in (b) reconstructed with CTX, (c) bottom right—scan in (b) reconstructed with PSBP. For all images: window = 1000 HU; level = −700 HU.

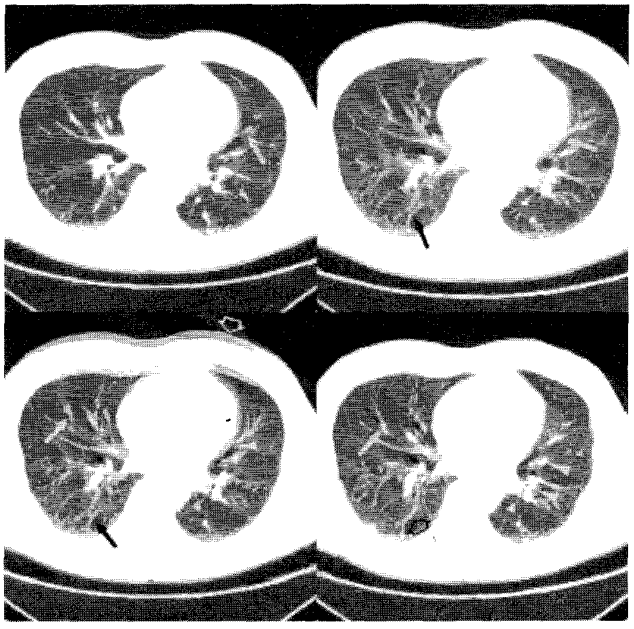

Fig. 9. Scans through the chest from volunteer 2: (a) top left—Scan during end-expiration, (b) top right—Scan during exhalation, (c) bottom left—scan in (b) reconstructed with CTX, and (d) bottom right—scan in (b) reconstructed with PSBP. For all images: window = 1000 HU; level = −700 HU.

vessels as shown in Fig. 8(b). The scan during exhalation reconstructed with CTX showed reduced doubling of the chest wall, but the vessels remain severely doubled (arrows), and the black patches remain (arrowheads) as shown in Fig. 8(c). The chest appears compressed because the CTX algorithm used the chest wall position at end-exhalation as the reference position. The scan during exhalation reconstructed with PSBP showed reduced doubling of the chest wall (arrow) and of the vessels in the right lung (arrowheads) as shown in Fig. 8(d). Vessels in the left lung were almost resolved into single structures (open arrows), but some slight doubling remained.

For the scans through the lung from the second volunteer, the scan at end-expiration showed well-defined vessels except near the moving heart wall (arrows) as shown in Fig. 9(a). The scan during exhalation reconstructed with a conventional algorithm showed minimal doubling of the chest wall, but severe doubling of the heart wall, and associated doubling of vessels (arrows) as shown in Fig. 9(b). The scan during exhalation reconstructed with CTX showed no noticeable reduction in doubling of the vessels (arrows) or heart wall (arrowhead), and added an additional distortion to the chest wall (open arrow) as shown in Fig. 9(c). The scan during exhalation reconstructed with PSBP showed a significant decrease in vessel (arrows) and heart wall doubling as shown in Fig. 9(d). Mediastinal structures in the left chest (arrowheads) are better defined, and doubling of vessels in the lower right chest is eliminated (open arrows). Doubling of the left and right heart walls and of vessels near the heart wall is nearly eliminated. Reconstructions with underscan did not noticeably improve the appearance of the images because large amounts of motion occurred throughout the scan.

A radiologist (JDG) who viewed the corrected images felt that the liver images and the CTX correction of the chest image showed no significant improvement, but that the PSBP-corrected lung images were improved enough to be useful.

VII. Summary

In this paper, we have shown that motion artifacts in CT scans can be reduced by applying the magnification and shift model of CTX on a local basis. CTX was able to correct artifacts that were caused by motion that fit the algorithm's motion model. However, this model poorly describes motion in the chest. Based on MRI correction methods in which correction was performed on a local basis, we assumed that local correction could also be used in CT. As shown by our results, altering the correction parameters for some sub-region of an image did not create artifacts such as streaks that contaminated other sub-regions. Although we cannot prove that no new artifacts were created, the fact that corrected images contained fewer artifacts than uncorrected images indicates that additional artifacts, if present, are less visible than artifacts caused by motion. Therefore, our assumption appears to be true for the few cases that we have shown here. Because PSBP allows for different parameters for each local region's magnification-and-shift model, PSBP is inherently more flexible than correction methods that are based on some global, parametric motion model.

To make PSBP useful, a method for estimating in-plane motion is required. Therefore, we developed a method for tracking the motion in the chest that used the acquired image

data. Although the motion-tracking method produced maps that enabled us to correct for motion, the method itself was not automated. Furthermore, application of the method was subjective, and we have no data on the reproducibility of the method's results. For research purposes, the motion-tracking method described here served its purpose. However, to make PSBP clinically applicable, the tracking process should be automated using an algorithm such as those described in [19] or [20].

Computer-simulated projections were reconstructed with PSBP to evaluate the algorithm. In the computer simulations, PSBP reconstruction introduced some streaking which was removed with underscan. This streaking could be caused by the fact that we assumed correction could be performed locally, by the fact that interpolation occurs in the implementation, or by the fact that we did not take into account the relationship between object magnification and the cutoff frequencies of the reconstruction kernel.

As shown by the corrections of the clinical images, some artifacts remained in the volunteer images after correction. These artifacts may not have been corrected for several reasons. First, motions that are impossible to correct for may be occurring. One example of such a motion is rotation that occurs at an angular frequency that is similar to that of the X-ray source. Second, S–I motion could be occurring. As noted in Section I, PSBP is unable to correct for this type of motion; S–I motion is most likely the predominant source of the artifacts in the liver scans. Third, inaccuracies in the output of the motion tracking method could lead to errors. Inaccuracies could occur from our assumption that the center-of-mass of an object represented its position, or from our assumption that the position of an object in a halfscan represented its average position. While these effects may be occurring, the fact that artifacts were reduced in clinical images indicates that these inaccuracies are of secondary importance.

In conclusion, we have shown that motion artifact correction can be performed on a local basis in CT. The ability to vary the correction parameters for individual pixels allows for better artifact correction than can be obtained with techniques that are based on global motion models. To further improve PSBP's performance, we could automate the motion tracking method, and extend the algorithm so that local motions consisting of translations, magnifications, and rotations can be corrected. Finally, one could consider attempting to perform motion correction in three dimensions by combining PSBP with helical scanning; for this application, the ability to track motion in the S–I direction would need to be developed. With these improvements, PSBP could become a tool that is clinically-useful for some patients.

ACKNOWLEDGMENT

The authors thank J. Hsieh, Ph.D., M. F. Gard, Ph.D., H. Levy, M.D., and W. Edwards, M.S.E.E. for their comments and suggestions on this manuscript.

REFERENCES

[1] J. D. Godwin, R. S. Breiman, and J. M. Speckman, "Problems and pitfalls in the evaluation of thoracic dissection by computed tomography," *JCAT*, vol. 6, pp. 750–756, 1982.

[2] L. R. Kuhns and G. Borlaza, "The twinkling star sign: An aid in differentiating pulmonary vessels from pulmonary nodules on computed tomograms," *Radiol.*, vol. 135, pp. 763–764, 1980.

[3] R. J. Alfidi, W. J. MacIntyre, and J. R. Haaga, "The effects of biological motion on CT resolution," *Amer. J. Radiol.*, vol. 127, pp. 11–15, 1976.

[4] R. D. Tarver, D. J. Conces, and J. D. Godwin, "Motion artifacts on CT simulate bronchiectasis," *Amer. J. Radiol.*, vol. 151, pp. 1117–1119, 1988.

[5] H. I. Goldberg, R. G. Gould, I. M. Feuerstein, J. S. Sigeti, and M. J. Lipton, "Evaluation of ultrafast CT scanning of the adult abdomen," *Invest. Radiol.*, vol. 24, pp. 537–543, 1989.

[6] C. J. Ritchie, J. Hsieh, M. F. Gard, C. R. Crawford, and Y. Kim, "Predictive respiratory gating: A new method to reduce motion artifacts in CT scans," *Radiol.*, vol. 190, pp. 847–852, 1994.

[7] N. J. Pelc and G. H. Glover, "Method for reducing image artifacts due to projection measurement inconsistencies," U.S. Patent 4,580,219, 1986.

[8] D. L. Parker, V. Smith, and J. H. Stanley, "Dose minimization in computed tomography overscanning," *Med. Phys.*, vol. 8, pp. 706–711, 1981.

[9] D. L. Parker, "Optimal short scan convolution reconstruction for fan-beam CT," *Med. Phys.*, vol. 9, pp. 254–257, 1982.

[10] C. R. Crawford, K. F. King, C. J. Ritchie, and J. D. Godwin, "Respiratory compensation in projection imaging using a magnification and displacement model," this issue, pp. 327–332.

[11] C. J. Ritchie, "Methods for reducing motion artifacts in computed tomography scans of the chest," Ph.D. dissertation, Univ. of Washington, Seattle, WA, 1993.

[12] E. M. Haacke and J. L. Patrick, "Reducing motion artifacts in two-dimensional Fourier transform imaging," *Magnet. Reson. Imag.*, vol. 4, pp. 359–376, 1986.

[13] R. L. Ehman and J. P. Felmlee, "Adaptive technique for high-definition MR imaging of moving structures," *Radiol.*, vol. 173, pp. 255–263, 1989.

[14] E. Atalar and L. Onural, "A respiratory motion artifact reduction method in magnetic resonance imaging of the chest," *IEEE Trans. Med. Imag.*, vol. 10, pp. 11–24, 1991.

[15] M. Hedley, H. Yan, and D. Rosenfeld, "A modified Gerchberg-Saxton algorithm for one-dimensional motion artifact correction in MRI," *IEEE Trans. Signal Processing*, vol. 10, pp. 1428–1433, 1991.

[16] J. B. West, *Respiratory Physiology—The Essentials*, 3rd ed. Baltimore, MD: Williams & Wilkins, 1985, p. 183.

[17] A. Maeda, K. Sano, and T. Yokoyama, "Reconstruction by weighted correlation for MRI with time-varying gradients," *IEEE Trans. Med. Imag.*, vol. 7, pp. 26–31, 1988.

[18] D. C. Noll, J. M. Pauly, C. H. Meyer, D. G. Nishimura, and A. Macovski, "Deblurring for non-2-D Fourier transform magnetic resonance imaging," *Magnet. Res. Med.*, vol. 25, pp. 319–333, 1992.

[19] G. Gerig, R. Kikinis, W. Kuoni, K. von Schulthess, and O. Kubler, "Semiautomated ROI analysis in dynamic MR studies–Part 1: Image analysis tools for automatic correction of organ displacements," *JCAT*, vol. 15, pp. 725–732, 1991.

[20] P. A. van den Elsen, E. D. Pol, and M. A. Viergever, "Medical image matching—A review with classification," *IEEE Eng. Med. Biol.*, vol. 12, p. 26, 1993.